Chinese Journal of Chemical Engineering 89 (2026) 25–35

Contents lists available at ScienceDirect

Chinese Journal of Chemical Engineering

journal homepage: www.elsevier.com/locate/CJChE

Full Length Article

Liquid–liquid two-phase flow and droplet formation in a T-junction microchannel

Nerisha Tuladhar , Muhammad Rafay Shahzad , Zien Huang , Sandeep Dhital , Taotao Fu *

State Key Laboratory of Chemical Engineering and Low-Carbon Technology, School of Chemical Engineering and Technology, Tianjin University, Tianjin 300072, China

ARTICLE INFO

Article history:
Received 23 July 2025
Received in revised form
21 September 2025
Accepted 22 September 2025
Available online 30 September 2025

Keywords:
Droplet formation
Interfacial phenomena
Liquid–liquid two-phase flow
T-junction microchannel

ABSTRACT

This study investigates the droplet formation for the liquid–liquid two-phase flow within a square T-junction microchannel through numerical simulation using volume of fluid method and experimental visualization using high-speed camera imaging. The T-junction microchannel has a cross-sectional width of 0.6 mm and a total length of 27.3 mm. The solution of cyclohexane with 2% and 3% mass concentrations of sorbitan trioleate surfactant were used as the continuous phase, and water was used as the dispersed phase. Slug flow, characteristic of squeezing regime, were predominantly observed. The effects of liquid–liquid two-phase flow rate ratio, and dimensionless number on droplet size, and pressure drop were investigated. The squeezing regime was mapped for $0.0005 \leq Ca_c \leq 0.0052$ (capillary number) and $0.1 \leq q \leq 10$ (flow rate ratio). The pressure drops of slugs were in the range from 40 Pa to 200 Pa. The slug lengths were measured between 1 mm and 9 mm. A universal flow map dependent on $Ca_cRe_d^{0.5}$ are projected to investigate the droplet formation behavior in T-junction microchannel. Correlation expressions are proposed to predict pressure drops and the slug lengths for liquid–liquid two-phase flow in a square T-junction microchannel, using dimensionless numbers such as flow rate ratio and capillary number. The result shows that large continuous phase flow rates facilitate smaller slugs, whereas higher dispersed phase flow rates result in longer shorts.
© 2025 The Chemical Industry and Engineering Society of China, and Chemical Industry Press Co., Ltd. All rights are reserved, including those for text and data mining, AI training, and similar technologies.

1. Introduction

Over the past decades, micro-chemical engineering has become an emerging technology that has transformative potential in vast areas like droplet-based emulsifications, chemical synthesis, and drug delivery, food-processing, biochemical engineering, and pharmaceuticals [1–4]. The microstructures wide utilization is because of its betterment in terms of mixing quality, microchannel control, and heat transfer due to high surface to volume ratio [5]. Microsystems excel in multiphase flows and research has greatly focused on understanding the phenomena of liquid–liquid and gas–liquid flows in microfluidic devices. To control and predict the flow behaviors, microdevices are essential in microchemical technology [6], because droplets or bubbles rarely cause coalescence in microfluidic systems [4]. Y- and T-junctions [6,7], co-flowing [8], geometry-dominated devices [9], and flow-focusing devices [7] produces consistent droplets but uniformity highly depends on microchannel geometry [6,10]. For Y- and T-junction, gas–liquid or liquid–liquid flow rate ratio (q) and capillary number (Ca) mainly control the droplet formation process [6,8] whereas two-phase inertia controls flow-focusing and co-flowing devices [7,8]. When two-phase liquids interact in a microchannel, body forces and interfacial tension between the microchannel and the flowing liquids will affect the droplets shape, and flow patterns [11]. Previous studies has observed slug droplets, and parallel flow mapped using superficial velocities of the dispersed phase and the continuous phase or using dimensionless numbers, in circular and rectangular microchannels [3,8]. Microchannel can continuously and efficiently produce monodispersed droplets for stable, consistent, and effectual liquid–liquid flow [12], that offers effective mass and heat transfer [5,10], high sensitivity [13], and improved controllability [14]. Therefore, microdevices are increasing popularity as it is simple to manufacture and easy to use [15].

Among microfluidic geometries for generating monodispersed droplets, the T-junction with a crossflow shear method is the most prevalent as it produces highly monodispersed droplets with

This article is part of a special issue entitled: Microchemical technology published in Chinese Journal of Chemical Engineering.

* Corresponding author.
E-mail address: ttfu@tju.edu.cn (T. Fu).

https://doi.org/10.1016/j.cjche.2025.09.009
1004-9541/© 2025 The Chemical Industry and Engineering Society of China, and Chemical Industry Press Co., Ltd. All rights are reserved, including those for text and data mining, AI training, and similar technologies.

uniform spacing. Thorsen *et al.* [16] initiated the idea of drop formation in multiphase flow and revealed that the droplet size in T-junction channels balances shear and interfacial forces, by providing a prediction model for force balance analysis. A model for slug size was developed by Garstecki *et al.* [17] valid for Ca_c <0.01. Further, several research have focused on the scaling law of droplet generation at low values of $Ca_c < 0.01$ [7,9,18,19]. Experimental and numerical simulations revealed crucial value of capillary number, that distinguished the technique of break-up and the observed flow regimes [20]. Building on these basic findings, it is significant to further investigate the slug flow characteristics because of its importance in improving interfacial transport. Moreover, numerous pressure drop correlations exist for circular and rectangular cross-sections [21,22]. Wong *et al.* [23] developed a modified form of Hagen–Poiseuille equation to express frictional pressure drop and an equation for interfacial pressure drop. Yet, the pressure drop models for a square cross-sectional microchannel are still scarce and should be addressed [24].

This paper aims to combine visualization experiments with volume of fluid (VOF) method numerical simulation to study the droplet formation and the fluid flow behavior of liquid–liquid flow in a squared T-junction microchannel. A universal flow pattern map is introduced by using $Ca_cRe_d^{0.5}$ composite dimensionless number to differentiate between slug, slug-drop, and long-slug flow patterns across broad conditional ranges. Additionally, a simplified non-film pressure drop model for squared T-junction microchannel is proposed. Also, this work clarifies the mechanisms of droplet formation in low capillary flow regimes and examines the effects of operating conditions such as the flow rate ratio of both phases, the rheological property of the continuous phase, and dimensionless numbers for liquid–liquid two-phase flow in microchannels. Finally, a predictive model for droplet size and pressure drops is established using dimensionless numbers, viscosity ratios, and fluid flow rate ratios. The correlations proposed in this study make setup easier by helping reduce trial and error and run operations smoothly.

2. Methodology

2.1. Experimental setup

The experiment was carried out by using deionized water as the dispersed phase and the solution of cyclohexane with 2% and 3% mass concentrations of sorbitan trioleate (span 85) surfactant as the continuous phase. The physical properties of Newtonian liquids such as the surface tension, density, and viscosity were taken from work done by He *et al.* [25] and are listed in Table 1. Flow viscosity was measured using a U's viscosity meter (iVisc, LAUDA, Germany), and the density was measured using a density meter (Anton Paar MA-4500-M, Austria). Also, a pendant drop method was used to measure surface tension, and a sessile drop process was used to measure contact angle values. The contact angles are measured for the continuous phase (cyclohexane with 2% or 3% span 85). The high contact angles are because of the presence of surfactants and also cyclohexane is hydrophobic in nature. In the simulation for continuous phase, these values are employed as boundary conditions. As water was the dispersed phase, which means that it did not wet the channel walls directly in the flow. Due to this reason, the contact angle on polymethyl methacrylate (PMMA) was not required.

Table 1
Physical properties of Newtonian fluids.

Fluid	Density, ρ/kg·m^{-3}	Viscosity, μ/mPa·s	Surface tension, σ/mN·m^{-1}	Contact angle, θ/(°)
Water	998.2	1.003	–	–
Cyclohexane + 3% (mass) span 85	783.6	1.060	9.52	146.8
Cyclohexane + 2% (mass) span 85	790.4	1.070	9.53	135.4

Two PMMA plate was used to fabricate the T-junction microchannel by precision machining, and the milling manufacturing error was ±1 μm. The upper and lower plates were mechanically sealed by bolts. The schematic structure of the microchannel used in this study is shown in Fig. 1(a). A is the inlet point for the dispersed phase, B is the inlet point for the continuous phase, and C is the outlet point of discarded fluids. The width (w) and length (l) of the T-junction channel are 0.6 mm and 27.3 mm, respectively. The hydraulic channel diameter (D_h) is the same as the channel width for a squared microchannel.

The experimental setup of the slug generation in the T-junction squared microdevice can be divided into four parts: microchannel, droplet collection chamber, and liquid phase input and output entrance. The first step was to check the air tightness system, and then the position of microchannel was adjusted. Next, the high-speed camera lens (high-speed camera: Photonfocus MV2-1280–640 Switzerland; microscope: TAMRON AF90mm F/2.8 Di SP, Japan) was positioned vertically over the microchannel to capture the experimental images and subsequently analyze the flow pattern of the immiscible liquids. To provide proper illumination, a light source (Philips 13629, Japan) is positioned underneath the microchannel device which is adjusted until a clear image was observed. In addition, both immiscible fluids were assumed to be incompressible, isothermal, and Newtonian, *i.e.* viscosity, density, and interfacial tension were constant throughout the flow process. After that, the dispersed phase fluids and continuous phase solutions were fed into the microchannel *via* two high-precision syringe pumps (PHD 2000, Harvard Apparatus, America) by carefully adjusting the desired liquid flow rates and directed to the T-junction microchannel. The volumetric flow rates were in the range from 100 to 1000 μl·min^{-1} for both the continuous and dispersed phase flow. The microdevice and the pumps were connected by a PVC tube. On every chosen condition of liquid–liquid flow rate, the two fluids meet at the junction point and continue to flow downstream of the main channel containing the continuous phase, and then the dispersed phase spontaneously breaks at the T-junction interface to produce droplets. The images were captured and recorded when the droplet formation was stable and upon reaching stability, each setting was maintained for approximately 2–3 min to ensure flow stability before capturing the image. The frame rate of image recording was controlled by 1000 frames per second. Computer programs were utilized to track records of experimental images and follow-up processing methods. Also, a collector vessel was set up to gather the discarded liquids. The experimental studies were performed under normal atmospheric pressure and the ambient temperature, and solution temperatures were maintained at 25 °C, which were regulated and monitored by air conditioners and thermometers, respectively. Subsequently, the continuous phase volumetric flow rate was maintained at a constant value, while the dispersed phase volumetric flow rate kept increasing gradually. The dimensionless numbers used in this study are capillary number (Ca), referred to as the ratio of the relative shear force to interfacial tension; Reynolds number (Re), defined by the relative magnitude ratio of inertial forces to viscous forces; and Weber number (We), defined by the relation between the interfacial forces and the relative magnitude of inertial forces, which are computed as $Ca = \mu c/\sigma$, $Re = \rho u D_h/\mu$, and $We = \rho u^2 D_h/\sigma$. In the experiment, the range of dimensionless numbers are as follows: $0.000515 < Ca_c < 0.005198$,

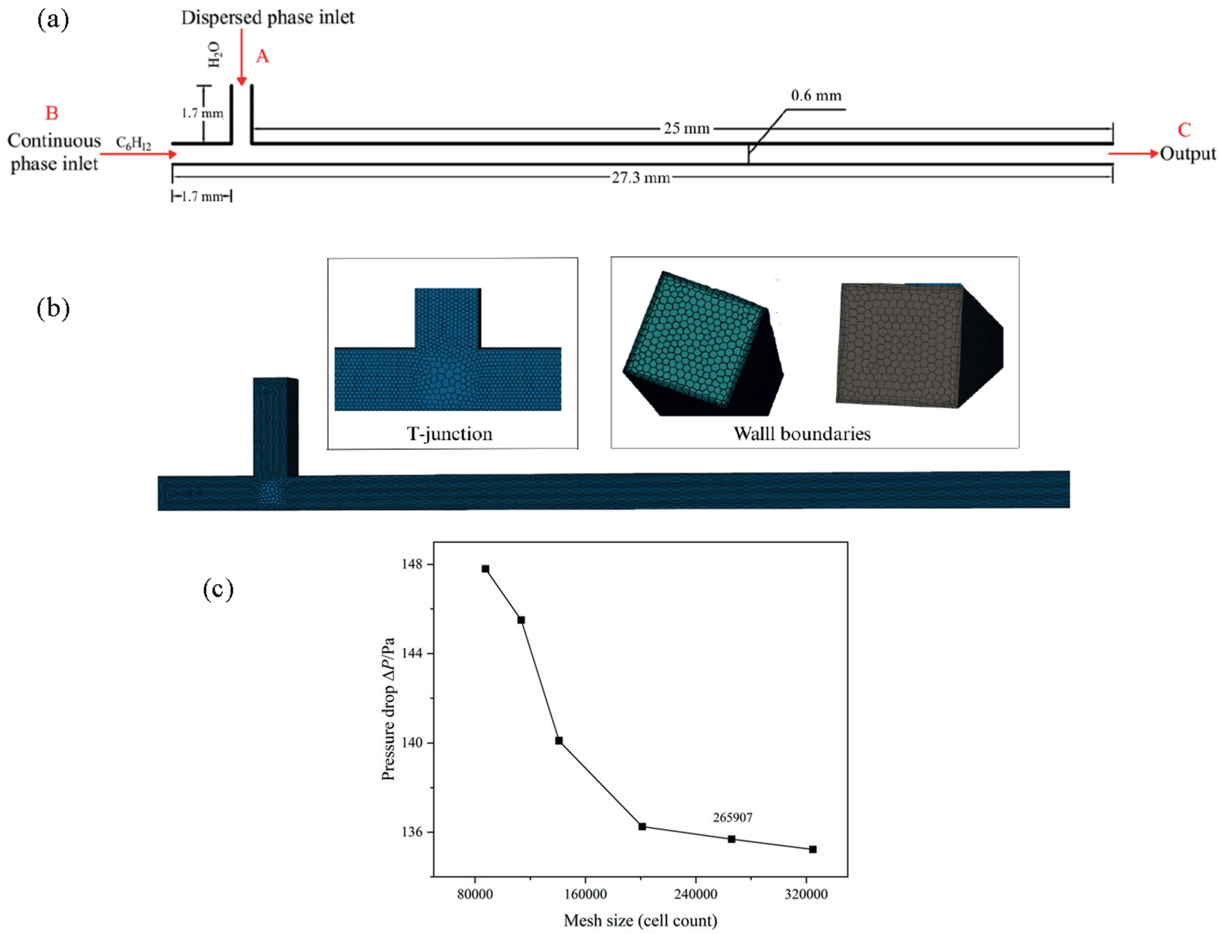

Fig. 1. (a) Structure of T-junction microchannel; (b) mesh image; (c) grid independent study.

$2.05192 < Re_c < 20.5346$, $0.001059 < We_c < 0.10666$; $0.000244 < Ca_d < 0.004878$, $1.3822 < Re_d < 27.644$, and $0.000337 < We_d < 0.134842$.

2.2. Numerical simulation

The 3-D geometry with two inlets and one outlet, forming a T-shaped junction with dimensions same as in the experimental setup, was created. The simulation was carried out using the volume of fluid method, where water-tight geometry was selected. Then, the model was meshed using a polyhedral mesh due to its better geometric adaptability and good meshing quality. All meshes were set with two boundary layer meshes near the walls to better capture the flow characteristics and improve the resolution of pressure and velocity gradients. Also, to ensure the stability of the simulation results and that they were not affected by mesh irrelevance, a grid independent study was done as shown in Fig. 1(c). Various grid sizes were tested, and the pressure drop was analyzed using volume-based simulations. The reported mesh count (260000) was chosen after the grid independence study. As the pressure drop remained stable at different mesh counts, we confirmed that this mesh size was enough for accurate simulation. The mesh image, along with the enlarged views at the wall boundaries and near the T-junction are shown in Fig. 1(b). A well-distributed element across the flow path demonstrates good mesh quality. The mesh refinement near the inlet, outlet, and junction regions ensures proper representation of flow features. Because the experiment did not use pressure indicators, the pressure drops were computed from the simulation between the model's input and output. After the meshing part, simulations were carried out using the volume of fluid method to track the interface between fluids. The laminar flow model was used to perform simulation under all tested conditions because the *Re* of the fluid flow in the microchannel was generally less than 2000, which is a typical laminar flow. For this study, changes in velocity were done to determine the results based on different conditions. The hybrid initialization was carried out after setting up all the initial values, such as the viscosity, density, surface tension, and contact angle of two phases. A transient (time-dependent) solver was used to properly simulate the dynamic nature of the droplet formation process. Simulation time step size and total run time were chosen according to flow stability and convergence behavior, and contour plots were checked throughout the computation process [19,26]. In this study, we assume that film thickness does not exist between the droplet and the channel wall because it simplifies the analysis and improves accuracy of the slug length calculations. It is a reasonable assumption for most VOF-based simulations of droplet flows as these simulations often do not model wall wetting and thin-film interactions, and makes the model easier and faster to solve, without affecting the accuracy of the main results [8,9].

To validate the accuracy of the numerical simulation outcomes, the comparison of the experimental results and the simulation predictions were done for slug length and pressure drop parameter under same flow conditions. These relationships are presented and examined in the Results and Discussion. The numerical model captured the major trends detected experimentally such as the decrease of slug length with increase in capillary number, and the increase of pressure drop with flow rate ratio. Even though there are small differences because of simplifications such neglecting thin films and assuming constant contact angles, the agreement is within the acceptable precision applications.

2.3. Governing equation

The governing equations for Newtonian fluid flows in the VOF method is described by the continuity and momentum equation, as shown in Eq. (1), and Eq. (2) respectively.

$$\nabla \cdot \boldsymbol{v} = 0 \tag{1}$$

$$P\left(\frac{\partial \boldsymbol{v}}{\partial t} + \boldsymbol{v} \cdot \nabla \boldsymbol{v}\right) = -\nabla p + \mu \nabla^2 v + f + R \tag{2}$$

where $\boldsymbol{v}$ is the velocity vector, ρ is the density of fluid, μ is the liquid viscosity, p is the pressure, R is the body force due to surface tension, and f is the component of the body force. The software incorporates two body force components R (surface tension) and f (another body force), which are added to momentum equations that affect fluid flow. The surface tension effects are calculated using the continuum surface force (CSF) model, where it is treated as a volumetric source based on surface tension coefficient. Other body forces are incorporated through pre-defined settings. These forces are significant to properly simulate physical effects on dynamics of fluid flow. In VOF approach, two or more phases are immiscible. Each phase is identified by a volume fraction α_i in a computational cell. For liquid–liquid systems, $\alpha_{\text{liquid-1}} = 1$ if the computational cell completely fills up phase-1, whereas if the cell is filled with phase-2, then $\alpha_{\text{liquid-2}} = 0$. The volume fractions between 0 and 1 represent the phase boundary in which the liquid-1 and liquid-2 interface exists. The sum of volume fractions of all phases equals to one. In this simulation study, $\alpha = 0$ for the continuous fluid (phase-1), and $\alpha = 1$ for dispersed liquid (phase-2).

Table 2
Accuracy of measuring equipment used in this experiment.

Experimental equipment	Measured quantity	Accuracy
Syringe pump	Volumetric flow rate (Q_c, Q_d)	±0.5%
High-speed camera	Slug length, droplet frequency	±1 pixel
T-junction microchannel	Channel width = 0.6 mm	±1 μm

2.4. Uncertainty analysis

Uncertainty and error analysis is critical for evaluating experimental findings with the lowest inconsistency. Uncertainty is defined as a lack of experimental measurement sureness that causes lack of certainty or complete loss of information. The accuracy of measuring equipment in this experiment, such as syringe pump, high-speed camera, and T-junction microchannel are specified by the manufacturers as shown in Table 2. The uncertainties associated with the majority of measured flow parameters are greatly affected by parameter magnitude [27].

Before proceeding with the procedure and results, we conducted an error analysis on out experimental observations in order to measure potential errors (W) associated with any computed flow parameter (E) by using the method described by Kline and McClintock [28].

$$W_E = \sqrt{\left(\frac{\mathrm{d}E}{\mathrm{d}y_1}w_1\right)^2 + \left(\frac{\mathrm{d}E}{\mathrm{d}y_2}w_2\right)^2 + \ldots + \left(\frac{\mathrm{d}E}{\mathrm{d}y_n}w_n\right)^2} \tag{3}$$

where w represents the uncertainty associated with a measured variable (y). The uncertainties in thermophysical parameters range from ±(0.5% to 5%), causing errors in dimensional as well as dimensionless groups including superficial velocity (uncertainty 0.54%–0.60%), and slug length (uncertainty 1.2%–2.4%).

3. Results and Discussions

3.1. Flow patterns in T-junction microchannel

Throughout the experiment, the dispersed phase flow rate was kept constant while gradually increasing the continuous phase flow rate. Under varying operating conditions, a total of 3 major flow patterns were observed in T-junction microchannels which are slug, long-slug, and slug-drop for both the systems containing 3% and 2% (mass) surfactant concentrations. The flow patterns observed for experimental and numerical methods are shown in Fig. 2. In slug flow, the continuous cyclohexane phase forms slugs that are separated by dispersed water droplets (Fig. 2(a)). In slug-drop flow, alternating water slugs and smaller water droplets are formed (Fig. 2(b)). In long slug flow, elongated water slugs occupy most of the channel's width, creating a continuous slug pattern with minimal space between slugs (Fig. 2(c)). The simulation results showed good agreement with experimental results. However, the experimental picture and simulation phase contour did not match in all cases. In experiments, there may be unforeseen system dynamics, such as changes in the flow due to

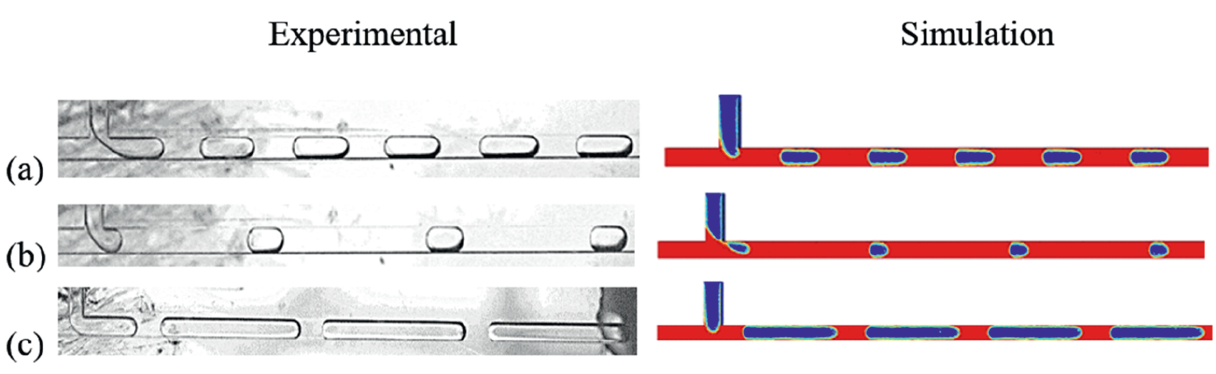

Fig. 2. Representative flow patterns of cyclohexane–water two-phase flow in square microchannels: (a) slug flow ($Q_c = 500$ μl·min^{-1}, $Q_d = 500$ μl·min^{-1}); (b) slug-drop flow ($Q_c = 300$ μl·min^{-1}, $Q_d = 100$ μl·min^{-1}); (c) long-slug flow ($Q_c = 100$ μl·min^{-1}, $Q_d = 400$ μl·min^{-1}).

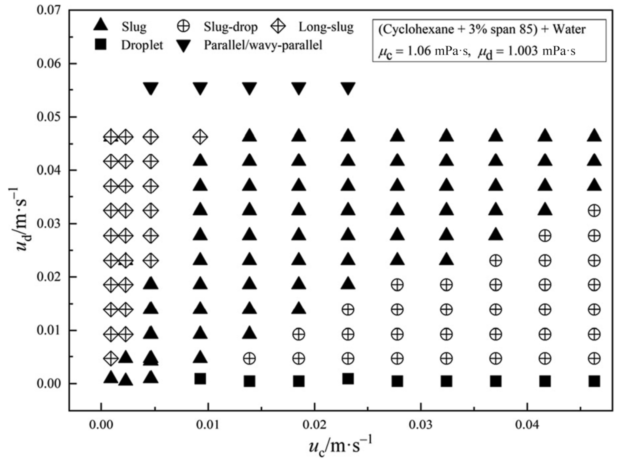

Fig. 3. Flow patterns map in square microchannel based on superficial velocity of the continuous and dispersed phases.

temperature or pressure variations that were not accounted for in the simulation. Also, viscosity and surface tension were constant for simulation study, while they could vary with surrounding temperatures or concentrations during the experiment.

The main flow regimes encountered in these experiments was the squeezing regime characterized by unique droplet formation dynamics. In the squeezing regime, the evolving droplet obstructs the channel width that will have some impact on the properties of fluid. This regime occurs when Ca_c<0.002 [26]. The droplet size was determined by the ratio between two phase flow rates, and they were normally longer than the width of the microchannel [17]. When Ca_c<0.002, the crossflow shear force exerted by the continuous fluid was significantly less than the interfacial force, which was not enough to break up the dispersed phase into slugs or drops. Therefore, the two-phase fluid flow produced a slug flow regime. In a squeezing regime, the interfacial force controls the shear force, and thus, the droplet break-up was influenced by the pressure drop across the slug during its formation. At relatively lower values of capillary numbers, the research observed only the squeezing regime within volumetric flow rates of 100 to 1000 μl·min^{-1} for both the Q_c and Q_d. At flow rates less than 100 μl·min^{-1} or more than 1000 μl·min^{-1}, other flow patterns like wavy parallel flow, and droplets flow were also observed that showed characteristics of the dripping regime, which was beyond the range of this study. Consequently, the analysis was confined to the squeezing regime, as it encompasses most of the observed data. Flow pattern maps are usually presented based on superficial velocities of the two phases or based on dimensionless numbers [29]. This work presents flow patterns based on superficial velocity ($u = Q/A$, as presented in Fig. 3. The slug flows dominated at higher Q_c or u_c values, while droplets and parallel flow were observed at moderate Q_c and higher Q_d.

Fig. 4(a) demonstrates that with an increase in Q_d, the flow transition lines moved upward, and with increasing Q_c, the flow pattern shifted from long-slug flow to slug, and later to slug-drop flow. Further, an increase in Q_c contributed to the flow pattern transition, and an increase in the Q_d prevented the droplets from entering the next flow pattern. Consequently, the transitions of flow pattern were highly affected by the liquid–liquid flow rates. Researchers found that different factors, including fluid viscosity, microchannel size, and interfacial tension are related to the flow pattern [30]. Consequently, it is not often suitable to split flow patterns just by independent dimensionless integers such as *Ca* or *Re*. The flow pattern transition of liquid–liquid two-phase flow in the convective T-junction microchannel was characterized by a composite dimensionless number produced in the form of *Ca*•*Re*. Lei *et al.* [30] presented an expression for the conversion boundary: $Ca_d^{0.7} Re_d^{0.5} = 0.385\,(Ca_c\, Re_c^{0.5})^{0.877}$. As demonstrated in Fig. 4(b), the expression also has an acceptable prediction in the present studies. The area above the line is the slug flow controlled by surface tension. As the dispersed phase velocity increases, the flow pattern will shift to the long slug flow which is dominated by the inertial force.

3.2. Slug droplets formed in the squeezing regime

Fig. 5(a) shows a four-stage breakup cycle that repeats every time a slug is generated in the squeezing regime. First, the newly formed slug moves forward, and the dispersed slug retracts rapidly after the slug pinch-off caused due to surface tension force, as demonstrated in Fig. 5(a1). This retraction is driven by *Ca* and helps to reduce the interfacial area by resetting the channel for the next cycle. Second, the dispersed slug radially and axially expands from the main channel as a result of continuous supply of the dispersed phase through the pump until a neck appears, as seen in the Fig. 5(a2)–(a4). In this phase, the drop predominantly fills the junction, partially obstructing the continuous phase flow, resulting in increased pressure in both side channels due to the ongoing flow of the aqueous phase. Therefore, the expansion stage t_e

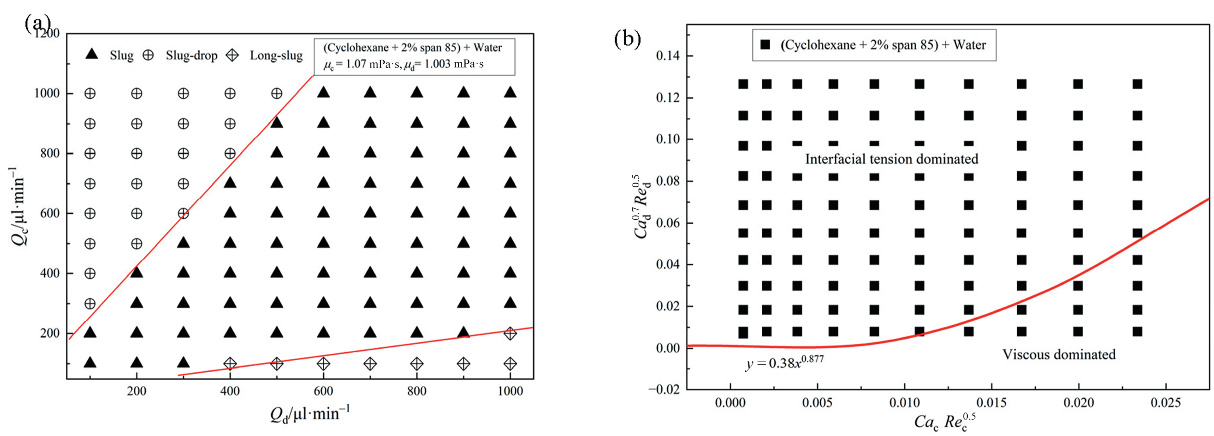

Fig. 4. (a) Flow pattern transition map; (b) Flow pattern of water–cyclohexane (2% span 85) with composite dimensionless numbers as coordinates.

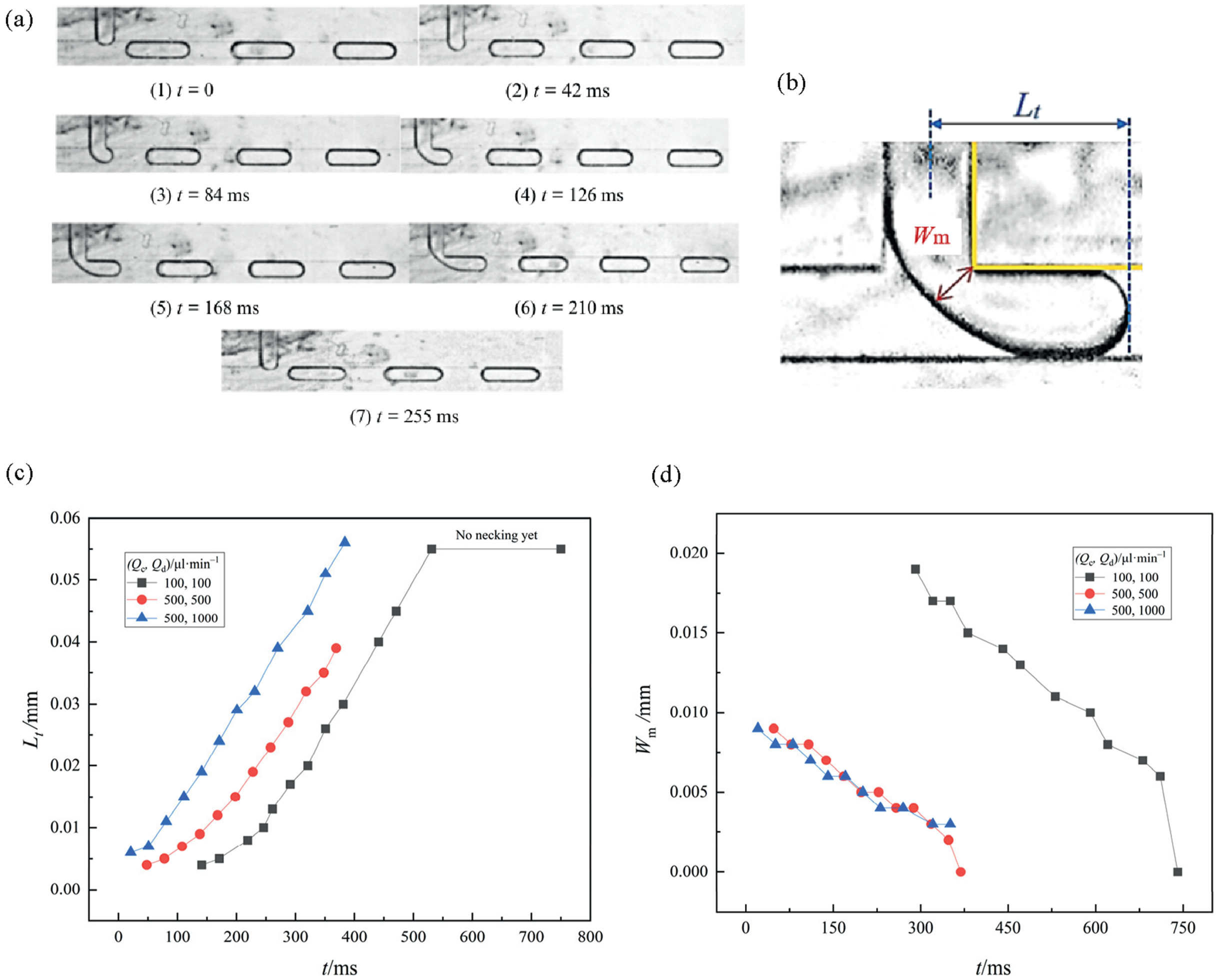

Fig. 5. (a) Droplet formation in the slug flow pattern, $Q_c = 500$ μl·min^{-1}, $Q_d = 500$ μl·min^{-1}; (b) schematic of the water–cyclohexane interface, the definitions of the minimum width W_m and the length L_t of the thread tip; (c) evolutions of the slug tip length L_t; and (d) the neck width W_m.

depends on junction volume and Q_d. After that, the accumulated pressure results in a reduction of the dispersed slugs in the radial direction while elongating it in the direction of axial movement, as illustrated in Fig. 5(a4)–(a6). The minimum slug neck width decreases as the collapsed time, t_c, progresses during the collapse stage. This collapse transforms the stored interfacial energy into kinetic energy, mostly opposed by viscous shear in the continuous phase, which explains why t_c is longer than t_e. Ultimately, as the neck narrows down, the shortest distance from the channel wall interface W_m decreases, leading to breaking up into slugs, as depicted in Fig. 5(a7). Thus, the dispersed slug subsequently retracts because of the surface tension force, which thereby creates a new droplet, and the pinch-off time t_p is relatively short.

The pinch-off mechanism could be quantitatively described by the temporal evolution of the tip and width of the neck as shown in Fig. 5(b). Fig. 5(c) shows the temporal change of the slug tip under three distinct environments. In the expansion stage, the growth of the slug is led by the dispersed phase. Both phases influence the development of the slug during the collapse stage. Thus, the collapse time t_c is more than the expansion time t_e and the rate of propagation of the slug tip in the earlier stage is slower than that in the subsequent one. Fig. 5 (d) displays the temporal development of the smallest distance between the neck and the wall. The variation of this distance is referred to as expansion for the first stage and collapse rate of the neck for the second stages. The neck's growth rate rises quickly in the first stage to achieve a maximum value; this time is slightly short. Then, this interval spans long enough and the neck's collapse rate reduces almost linearly approaching the pinche-off. The liquid flow rates define the collapse rate of the droplet neck. The collapse rate of the neck rises as the liquid flow rate rises. For clarity, both the slug-tip length and the minimum neck width are extracted from the same high-speed camera and in the same time span. L_t starts from $t = 0$ whereas W_m is not defined until the neck appears. The horizontal straight line marks the no necking zone where the position of slug-tip remained same before pinch-off. For low values of Q_c, and Q_d, the pre-neck interval is longer which is reason W_t is recorded almost 150–300 ms later than L_t. At higher values of Q_c and Q_d, however, the pre-necking window is much shorter, so the neck is visible almost immediately. Increasing Q_c reduces both the t_e and t_c, while larger Q_d stretches t_e and generates longer slugs. Consequently, Q_d, primarily controls slug size and Q_c determines production frequency. Excessively long slugs increase pressure drops and can block channels, whereas low Q_c induces bypass flow and reduces monodispersity.

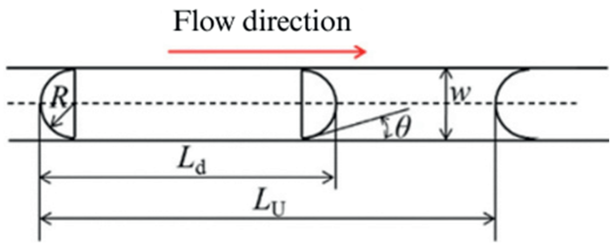

Fig. 6. Flow in microchannel without film.

3.3. Factors affecting droplet size

The slug length is affected by the flow rate ratio of both phases, and capillary number [11]. By neglecting the film, it facilitates more precise estimation of slug length and characterizes flow accurately. A typical droplet shape and size without liquid films is given in Fig. 6, where L_d, L_U, w, R, and h denotes droplet length, unit length of drops, microchannel width, radius of droplet cap, and thickness of liquid film, respectively. As seen in Fig. 6, the droplet is regarded as a regular cube paired with a hemisphere [31]. In this study, the channel interface is square. So, the droplet can be considered as consisting of two hemispheres and a cuboid which is expressed as:

$$\text{Surface area} = (\pi - 2\theta)\frac{w^2}{4\cos^2\theta} + 4w\left(L_d - \frac{w}{\cos\theta} + w\tan\theta\right) \tag{4}$$

Fig. 7(a) shows the relationship between the flow rate ratio and dimensionless slug length (L/w). At fixed Q_d, the length of slug increases with an increase in flow rate ratio. Slugs grow longer at higher Q_d/Q_c because weaker shear allows elongation before pinch-off. At lower flow rate ratios (<2), the slug lengths are relatively small for both systems, but as the ratio increases (>2), the weak shear environment leads to faster elongation and the slug length grows more rapidly [29]. This shows that dispersed phase flow governs slug size, while continuous phase influences breakup frequency. The predictive equations for the droplet lengths on the basis of flow rate ratios are as follows:

$$L/w = 1.24 + 1.86q \tag{5}$$

where L/w denotes dimensionless droplet length; w means channel width (mm); q is the liquid–liquid flow rate ratio (Q_d/Q_c). Fig. 7 (b) shows the variation of dimensionless slug length and continuous phase capillary number for cyclohexane-water system: L/w decreases with increasing Ca_c. This indicates that the rise in

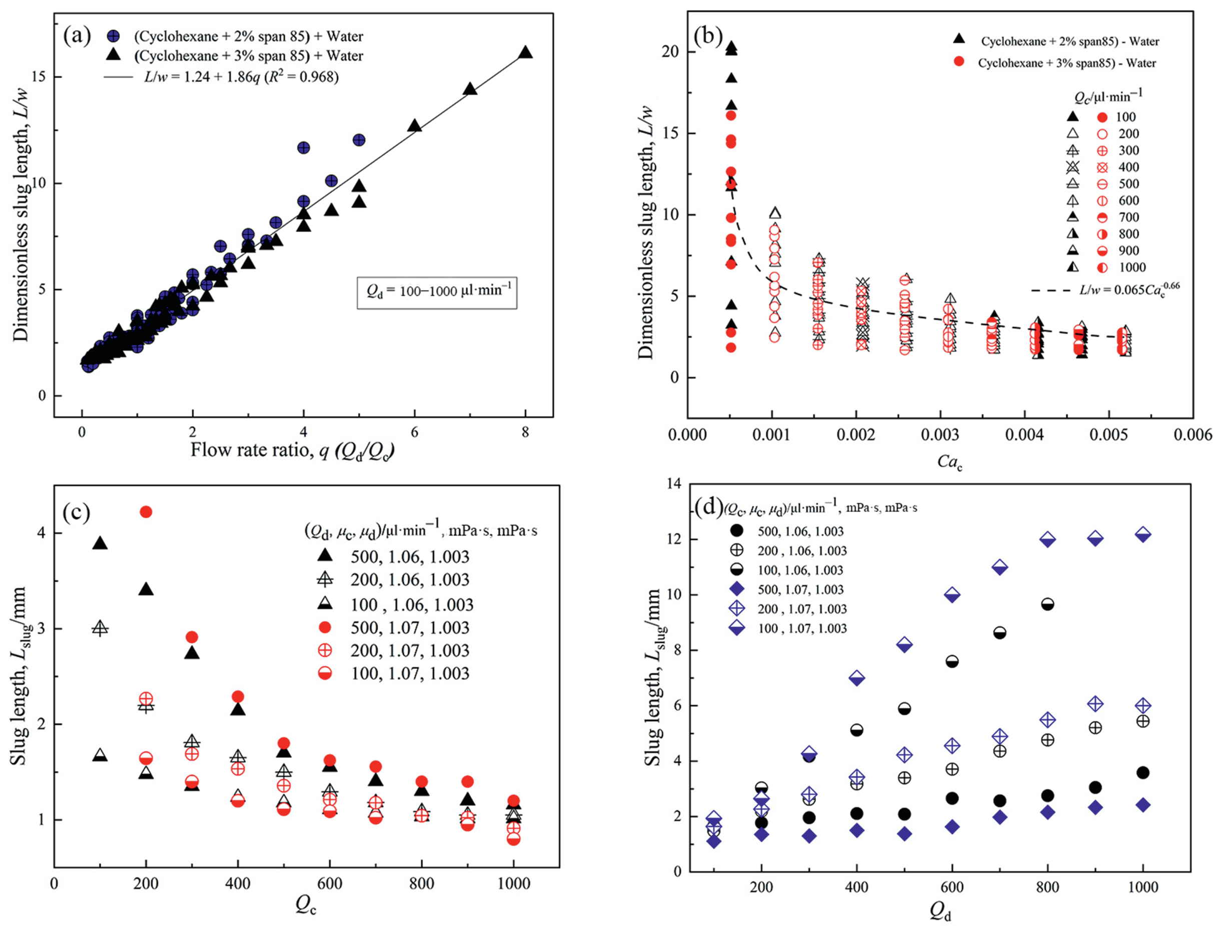

Fig. 7. Dimensionless slug length as a function of (a) flow rate ratio, and (b) the capillary number. Influences of (c) Q_c and (d) Q_d on droplet length.

capillary number increases the viscous force, which accelerates neck thinning; hence, the interface experiences high shear stress that results in a faster breakup producing shorter slugs [29]. Higher Ca_c reduces slug size but also increases pressure drop, which can be a drawback in long channels. By using a power law with a negative coefficient, the relationship between L/w and Ca_c can be developed effectively.

$$L\,/\,w = 0.065\ Ca_c{-}0.66 \tag{6}$$

Over a wide range of dispersed and continuous phase flow rates, this process produces uniform droplets [17]. The volume of these droplets can be adjusted by changing the flow rates of both phases. Fig. 7(c) and (d) signifies this dependence of the continuous and dispersed phase flow rate on slug length. The L_{slug} decreases as the continuous phase flow rate increases, whereas the slug size increases as the flow rate of the dispersed phase increases. Larger Q_c increases shear at the T-junction and reduces the filling time, resulting in early pinch-off and shorter slugs. Higher Q_d blocks the channel and pinch-off is delayed, resulting in longer slugs. Shorter slugs enhance mixing and interfacial areas, whereas longer slugs favor processes that require extended phase contact. However, longer slugs increase pressure loss and may reduce stability of flow. These trends aligned with the balance between inertial forces driving slug growth and viscous shear forces inducing breakup, for slug flow regimes in two-phase systems [17]. This indicates that the sizes of the droplets formed in a T-junction depend on the flow rates of both phases. For the squeezing regime under $Ca_c < 0.0058$, the flow formation was affected by the leakage flow which is dependent on Ca_c and q [32]. The empirical expression for the squeezing regime is derived, and it properly aligns with the experimental results when $Ca_c < 0.0058$, as shown in Eq. (6).

Unlike the study by Ma *et al.* [32], that utilized film thickness correlations to elucidate the deviations from the ideal squeezing regime, the present analysis did not utilize any effects of film thickness in the droplet length prediction. However, the proposed empirical equation demonstrated strong predictive performance under the experimental conditions, reinforcing that the squeezing regime dominates for the tested Ca_c range. Etminan *et al.* [33] simulated Taylor flow in an axisymmetric circular entrance and observed that high viscosity ratio stabilizes the interface and shortens liquid–liquid slugs. Qualitatively, these trends agree with our findings on squared T-junction microchannel, where L/w increases with q and decreases with Ca_c. Moreover, the slug length empirical correlations observed in this study follow similar forms compared to existing literature, by typically relating L/w to q and Ca_c [17,34–36], but they differ in the pre-factors and the fitted exponents.

3.4. Factors affecting pressure drop

In this section, we analyze the effect of capillary numbers on pressure drop within the T-junction microchannel during slug formation. Laminar flows dominate in microchannels and are characterized by the parabolic velocity profile. Interfaces present in multiphase flows disturb this velocity profile resulting in additional pressure losses defined as the interfacial pressure drop. In liquid droplets, the main contribution towards pressure drops are droplets and not thin films [37]. In this study, the pressure drops measurements of water–cyclohexane (3% span 85) and water–cyclohexane (2% span 85) system's slug flow generated in T-junction microchannel were carried out. The Hagen–Poiseuille's pressure drop equation in multiphase fluid flow in microdevices is expressed as:

$$\Delta P = \Delta P_{\text{frictional}} + \Delta P_{\text{interface}} \tag{7}$$

For liquid–liquid immiscible slugs, the pressure differences can be computed employing the Hagen–Poiseuille Law developed by Wong *et al.* [23] which describes the frictional pressure drop for laminar flow in pipes of circular cross-section, for laminar flow, which is free of liquid film layering the droplets, and is expressed as:

$$\Delta P = \Delta P_{\text{f,c}} + \Delta P_{\text{f,d}} + \Delta P_{\text{interface}} \tag{8}$$

where, $\Delta P_{f,c}$, $\Delta P_{f,d}$ means frictional pressure drop in the continuous and dispersed phase fluids, respectively. Mortensen and Okkels [38] developed and enhanced Hagen–Poiseuille equation applicable to non-circular geometries by introducing a dimensionless geometrical correction factor α. In this study, the equation was adapted for a non-circular microchannel as applied by Wong *et al.* [23] for interfacial and Mortensen and Okkels [38] for frictional pressure drop. For a square microchannel, ΔP due to laminar flow can be projected using the following formula:

$$\Delta P_{\text{frictional}} = \frac{12\mu LQ}{A^4} \tag{9}$$

The universal correlation for the interfacial pressure drop is expressed as:

$$\Delta P_{\text{interface}} = \frac{2\sigma}{D_h}\ c_1 Ca_d^{\frac{2}{3}} \tag{10}$$

This expression serves as a foundation for a no-film pressure drop model, where c_1 denotes a constant value that depends on the microchannel structure, capillary number, and droplet size. The slug droplets obtained in this work satisfy the criteria $2L_d/D_h < Ca_d^{-1}$ for which $c_1 = 3.553$ [23]. This criterion was satisfied under the present experimental conditions. The non-film model treats each droplet as a slug that completely fills the cross-section of the squared microchannel and moves with the average mixture velocity. Thus, the continuous phase is assumed to flow only in the slugs between droplets [37]. When no film is present, the equilibrium mass balance is streamlined, resulting in the velocity of droplet as $u_d = U$. Here, U represents the droplet velocity which under these conditions corresponds to superficial velocity of droplet phase. Capillary number is expressed as $Ca = \mu U/\sigma$, and cross-section area of droplet as $A_d = A$. Then, the subsequent correlation expression is acquired:

$$\frac{\Delta P}{L} = \alpha \frac{\mu_c U_c}{A}\left(1 + \frac{U_d \mu_d}{U_c \mu_c} + \frac{w+h}{\alpha}\ \frac{f_d}{U_c}\ c_1 Ca^{-1/3}\right) \tag{11}$$

where α is a dimensionless geometrical correction factor used for non-circular geometry. For a square microchannel, the correction factor is expressed as [37]:

$$\alpha = \frac{22}{7}\ \frac{P^2}{A} - \frac{65}{3} \tag{12}$$

The non-film predictions are plotted with the simulation data in Fig. 8. In Fig. 8(a), the pressure drops increases with the flow rate ratio for all continuous flow rates. As the flow rate of water rises from 100 to 300 $\mu l \cdot min^{-1}$, the pressure drop rises significantly for higher flow rate ratios because of stronger hydrodynamics forces. This shows that long slugs formed at higher q add larger viscous and interfacial resistance, explaining the observed increase in ΔP. For most experimental series, pressure drop increases linearly with the total flow rate [21]. Fig. 8(b) shows that the pressure drop similarly increases with the average flow velocity, showing a linear trend. This is because as average velocity increases, the wall shear in the laminar flow rises linearly, so friction loss will increase thus resulting in

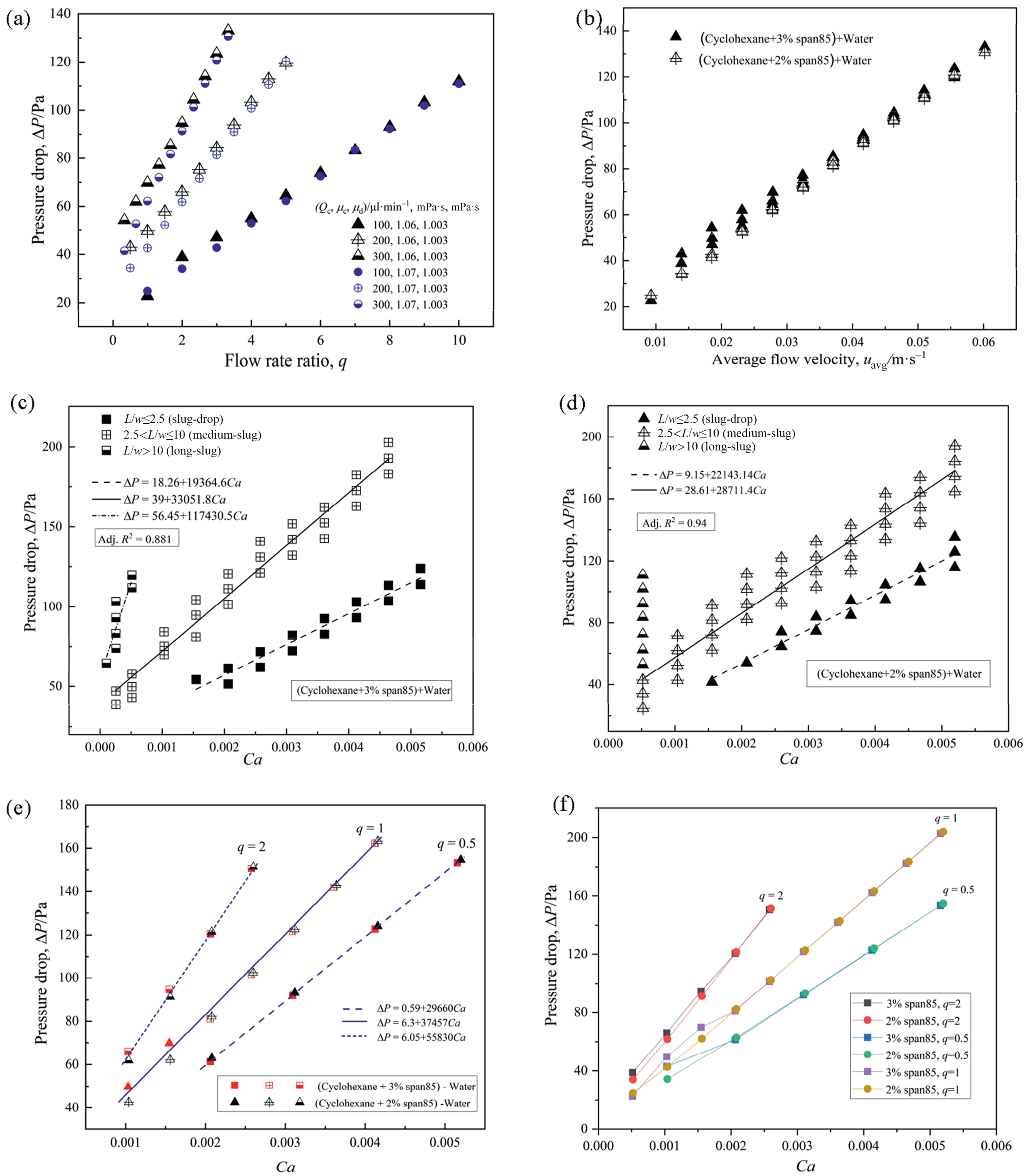

Fig. 8. Pressure drop as a function of (a) flow rate ratio, (b) average flow velocity, (c–d) capillary number for cyclohexane – 3% and 2% span 85, (e) capillary number under various flow rate ratio, and (f) capillary number under different surfactants.

higher pressure drops. Ladosz and von Rohr [37] found that the increase in pressure drop was dependent on the flow rate ratio and velocity. This behavior emphasizes the importance of shear force under low capillary number conditions, where interfacial tension controls pressure behavior and under high capillary number conditions, where viscous shear becomes dominant, as shown in Fig. 8(c) and (d). The linear trend confirms the validity of the correlation in the squeezing regime. This result supports the work by Garstecki *et al.* [17], who verified that in the squeezing regime, pressure-driven droplet formation exhibits a linear dependence on *Ca*, and the ratio of flow rates is fundamental to droplet properties. Long slugs exhibit the highest-pressure drops due to increased viscous and interfacial contributions from elongated slugs, while slug-drop cases result in lower pressure drops, which agrees with the research of Etminan *et al.* [6] and Kurimoto *et al.* [24]. Fig. 8(e) and (f) explains a linear correlation between the pressure drop and the capillary number in the squeezing regime as in Ref. [24]. For both systems, higher flow rate ratios led to increased pressure drops due to longer slug lengths and greater flow resistance, yielding the highest ΔP. Notably, the gap between pressure drop curves widens with increasing q, emphasizing the combined effects of surfactants and flow rate ratio. This highlights the advantage of adjusting surfactant concentration to reduce interfacial stress, although droplet stability may be affected by high q values. The constant c_1 in Eq. (11) may also vary depending on specific flow conditions, further contributing to the observed differences.

The non-film model makes the following assumptions [37]: (i) the droplet is not deformable and it perfectly occupies the square channel, (ii) the droplet velocity is equal to the average velocity of two-phase flow, (iii) the interfacial pressure drop is only affected by the hemispherical cap, and (iv) corner flow is neglected. The non-film model allows easy and quick estimates of pressure drop without the need to assume the thickness of liquid-film [37]. For liquids with viscosities that differ by less than one order of magnitude (which is common in lab-on-chip-devices), the model can make pressure drop predictions within an acceptable range [37]. This approach is practical for designing microfluidic devices. However, the systems with high viscosity, the model may underestimate ΔP. Therefore, this model is dependable for fluids exhibiting analogous viscosities and at low Ca but should be used carefully when viscosity of dispersed phase is higher than that of the continuous phase. Moreover, the pressure drops empirical correlations observed in this study follow similar trends compared to existing literature where ΔP increases with Ca and q [18,22]. Unlike previous models that incorporate film thickness, the current study focuses on no-film pressure drop model that directly accounts for operating parameters and droplet geometry. This model works better with experimental results in low-Ca regimes.

4. Conclusions

The liquid–liquid two-phase flow and droplet formation in a square T-junction microchannel was experimentally visualized using a high-speed camera and numerically analyzed using VOF. The two-phase flow patterns, the hydrodynamics in the squeezing regime, and the factors affecting slug length and pressure drop in the T-junction microchannel are studied. The droplet formation can be distinguished into three flow patterns: slug flow, slug-drop flow, and long-slug flow, and the breakup process was further classified into different stages such as waiting, filling, necking, and breaking which offers new perceptions into droplet dynamics. The influence of other flow types is explained by adapting composite terms ($Ca_d Re_d^{0.5}$) to form a universal flow map showing the occurrence of slug flow.

Furthermore, analysis on slug size and pressure drops were carried out along with the derived equations to validate the experimental and simulation outcomes with the predicted values. The slug lengths were observed to range from 1 to 9 mm, and the pressure drops were found ranging from 40 Pa to 200 Pa. The slug size was simply correlated by the liquid–liquid flow rate ratio and increasing capillary number shortened slug length because of the higher shear stress and stronger viscous forces. A non-film pressure drop model for square channels was employed using the frictional and interfacial pressure drop, which showed strong predictive performance.

This study was performed at room temperature, even though some liquid properties such as viscosity and surface tension are temperature sensitive. Cyclohexane was used as simple fluid, while many industrial applications exhibit more complex rheological behaviors. To improve applicability, further research should extend the analysis to complex fluids and incorporate parallel scaling experiments and simulations. Moreover, this study focused on droplet formation at the T-junction, which shows diverse flow patterns but limited operational range. The small parameter differences under varying two-phase flow rates made data analysis challenging. Future studies should explore stronger shear force, considering channel design and operational conditions to expand the droplet flow patterns in multiple channel systems and reduce the adverse effects of rheology on droplet stability. This work will help to understand the droplet dynamics in a microchannel, which will contribute to the industrial processes like chemical reaction and mass transfer at microscale.

CRediT Authorship Contribution Statement

Nerisha Tuladhar: Writing – review & editing, Writing – original draft, Methodology, Investigation, Formal analysis, Data curation, Conceptualization. Muhammad Rafay Shahzad: Writing – review & editing, Investigation. Zien Huang: Writing – review & editing, Investigation. Sandeep Dhital: Writing – review & editing, Investigation. Taotao Fu: Writing – review & editing, Supervision, Resources, Project administration, Funding acquisition, Conceptualization.

Declaration of Competing Interest

The authors declare that they have no known competing financial interests or personal relationships that could have appeared to influence the work reported in this paper.

Acknowledgement

The financial supports for this project from the National Natural Science Foundation of China (22378295).

Nomenclature

A	area, m^2
c	collapsed stage
D_h	hydraulic channel diameter, mm
E	computed flow parameter
e	expansion stage
h	channel height, mm
l	channel length, mm
l_h	head distance, mm
l_d	droplet length, mm
L_{slug}	slug length, mm
L_U	unit length of droplet, mm
L/w	dimensionless slug length
P	system pressure drops, Pa
P'	Perimeter, mm
ΔP	system pressure drop change, Pa
ΔP_I	interfacial pressure drops, Pa
q	flow rate ratio, dimensionless
Q_c	continuous phase flow rate, $\mu l \cdot min^{-1}$
Q_d	dispersed phase flow rate, $\mu l \cdot min^{-1}$
R	body force due to surface tension
r	radius, mm
t	time, ms
U	average fluid velocity, $m \cdot s^{-1}$
u	superficial velocity, $m \cdot s^{-1}$
V	droplet volume, mm^3
W	potential error
w	channel width, mm
w_m	minimum neck width, mm
w_n	uncertainty
α	phase fraction, dimensionless
ρ	density, $kg \cdot m^{-3}$
σ	surface tension/interfacial force, $N \cdot m^{-1}$
μ	viscosity, mPa·s
θ	contact angle, (°)

v velocity vector

Subscripts

avg average
c continuous phase fluid
d dispersed phase fluid
e expansion
f,c frictional force in continuous phase
f,d frictional force in dispersed phase
p pinch-off

References

[1] B. Rostami, G.L. Morini, Generation of newtonian droplets in newtonian and non-newtonian carrier flows in micro T-junctions under opposed-flow configuration, *J. Non Newton. Fluid Mech.* 281 (2020) 104297.
[2] G.T. Vladisavljević, E.E. Ekanem, Z.L. Zhang, N. Khalid, I. Kobayashi, M. Nakajima, Long-term stability of droplet production by microchannel (step) emulsification in microfluidic silicon chips with large number of terraced microchannels, *Chem. Eng. J.* 333 (2018) 380–391.
[3] A.A. Yagodnitsyna, A.V. Kovalev, A.V. Bilsky, Flow patterns of immiscible liquid–liquid flow in a rectangular microchannel with T-junction, *Chem. Eng. J.* 303 (2016) 547–554.
[4] A. Krishnan, V.K. Dhir, Numerical study of influence of lateral bubble merger on bubble dynamics and heat transfer during nucleate pool boiling on a horizontal substrate under a constant imposed heat flux, *Int. J. Heat Mass Transf.* 247 (2025) 127063.
[5] B. Huang, H. Li, S. Xia, T. Xu, Experimental investigation of the flow and heat transfer performance in micro-channel heat exchangers with cavities, *Int. J. Heat Mass Transf.* 159 (2020) 120075.
[6] A. Etminan, Y.S. Muzychka, K. Pope, Numerical investigation of gas–liquid and liquid–liquid Taylor flow through a circular microchannel with a sudden expansion, *Can. J. Chem. Eng.* 100 (7) (2022) 1596–1612.
[7] P. Chaudhary, S. Ghosh, An experimental and numerical investigation to study slug characteristics in miniature geometries, *Int. J. Multiph. Flow* 191 (2025) 105342.
[8] R. Abiev, S. Svetlov, S. Haase, Hydrodynamics and mass transfer of gas–liquid and liquid–liquid Taylor flow in microchannels, *Chem. Eng. Technol.* 40 (11) (2017) 1985–1998.
[9] A. Etminan, Y.S. Muzychka, K. Pope, Liquid film thickness of two–phase slug flows in capillary microchannels: a review paper, *Can. J. Chem. Eng.* 100 (2) (2022) 325–348.
[10] F.S. Al-Gburi, F. Khaleel, Y. Ding, J. Stofford, Numerical investigation of heat transfer in nanoparticle-enhanced Taylor flow using thermal MPPICInter-IsoFOAM, in: The 20th Open FOAM Workshop (OFW20), Vienna, Austria, 2025.
[11] J.Y. Qian, X.J. Li, Z. Wu, Z.J. Jin, B. Sunden, A comprehensive review on liquid–liquid two-phase flow in microchannel: flow pattern and mass transfer, *Mircofluid. Nanofluid.* 23 (10) (2019) 116.
[12] Z.M. Liu, Y. Yang, Influence of geometry configurations on the microdroplets in flowfocusing microfluidics, *Chin. J. Theor. Appl. Mech.* 48 (4) (2016) 867–876.
[13] D.A. Hoang, C. Haringa, L.M. Portela, M.T. Kreutzer, C.R. Kleijn, V. van Steijn, Design and characterization of bubble-splitting distributor for scaled-out multiphase microreactors, *Chem. Eng. J.* 236 (2014) 545–554.
[14] S.G. Sontti, A. Atta, CFD analysis of Taylor bubble in a co-flow microchannel with Newtonian and non-Newtonian liquid, *Ind. Eng. Chem. Res.* 56 (25) (2017) 7401–7412.
[15] C.Q. Yao, Y.Y. Liu, C. Xu, S.N. Zhao, G.W. Chen, Formation of liquid–liquid slug flow in a microfluidic T-junction: effects of fluid properties and leakage flow, *AIChE J.* 64 (1) (2018) 346–357.
[16] T. Thorsen, R.W. Roberts, F.H. Arnold, S.R. Quake, Dynamic pattern formation in a vesicle-generating microfluidic device, *Phys. Rev. Lett.* 86 (18) (2001) 4163–4166.
[17] P. Garstecki, M.J. Fuerstman, H.A. Stone, G.M. Whitesides, Formation of droplets and bubbles in a microfluidic T-junction: scaling and mechanism of break-up, *Lab Chip* 6 (3) (2006) 437–446.
[18] L. Ma, Z.F. Yan, C.C. Du, J. Deng, G.S. Luo, Effect of viscosity on liquid–liquid slug flow in a step T-junction microchannel, *Ind. Eng. Chem. Res.* 61 (23) (2022) 8333–8345.
[19] J.Y. Qian, X.J. Li, Z. Wu, Z.J. Jin, J.H. Zhang, B. Sunden, Slug formation analysis of liquid–liquid two-phase flow in T-junction microchannels, *J. Therm. Sci. Eng. Appl.* 11 (5) (2019) 051017.
[20] A. Etminan, Y.S. Muzychka, K. Pope, A review on the hydrodynamics of Taylor flow in microchannels: experimental and computational studies, *Processes* 9 (5) (2021) 870.
[21] A. Ładosz, E. Rigger, P. Rudolf von Rohr, Pressure drop of three-phase liquid–liquid–gas slug flow in round microchannels, *Microfluid. Nanofluid.* 20 (3) (2016) 49.
[22] A. Abdollahi, S.E. Norris, R.N. Sharma, Pressure drop and film thickness of liquid–liquid Taylor flow in square microchannels, *Int. J. Heat Mass Transf.* 156 (2020) 119802.
[23] H. Wong, C.J. Radke, S. Morris, The motion of long bubbles in polygonal capillaries. Part 1. thin films, *J. Fluid Mech.* 292 (1995) 71–94.
[24] R. Kurimoto, K. Hayashi, A. Tomiyama, Pressure drop and bubble velocity in Taylor flow through square microchannel, *Microfluid. Nanofluid.* 28 (8) (2024) 58.
[25] C.X. He, B. Jiang, W. Zhan, S.C. Li, X.D. Wang, C.Y. Zhu, Y.G. Ma, T.T. Fu, Mesoscale effect on droplet formation in a step-emulsification microdevice with parallel microchannels, *Chem. Eng. J.* 454 (2023) 140275.
[26] W. Khan, A.K. Chandra, K. Kishor, S. Sachan, M.S. Alam, Slug formation mechanism for air–water system in T-junction microchannel: a numerical investigation, *Chem. Pap.* 72 (11) (2018) 2921–2932.
[27] A. Etminan, Y.S. Muzychka, K. Pope, Experimental and numerical analysis of heat transfer and flow phenomena in Taylor flow through a straight mini-channel, *ASME J. Heat Mass Transf* 145 (8) (2023) 081801.
[28] S.J. Kline, The purpose of uncertainty anaslysis, *J. Fluids Eng.* 107 (2) (1985) 153–160.
[29] Z. Wu, Z. Cao, B. Sundén, Liquid–liquid flow patterns and slug hydrodynamics in square microchannels of cross-shaped junctions, *Chem. Eng. Sci.* 174 (2017) 56–66.
[30] L. Lei, Y.T. Zhao, W.K. Chen, H.L. Li, X.Y. Wang, J.Z. Zhang, Experimental studies of droplet formation process and length for liquid–liquid two-phase flows in a microchannel, *Energies* 14 (5) (2021) 1341.
[31] M. Sattari-Najafabadi, M. Nasr Esfahany, Z. Wu, B. Sundén, Hydrodynamics and mass transfer in liquid–liquid non-circular microchannels: comparison of two aspect ratios and three junction structures, *Chem. Eng. J.* 322 (2017) 328–338.
[32] H.Y. Ma, Q.K. Zhao, C.Q. Yao, Y.C. Zhao, G.W. Chen, Effect of fluid viscosities on the liquid–liquid slug flow and pressure drop in a rectangular microreactor, *Chem. Eng. Sci.* 241 (2021) 116697.
[33] A. Etminan, Y.S. Muzychka, K. Pope, CFD Modelling for gas-liquid and liquid–liquid Taylor Flows in the Entrance Region of Microchannels. In: ASME 2021 Fluids Engineering Division Summer Meeting, 2021.
[34] T.A. Prileszky, B.A. Ogunnaike, E.M. Furst, Statistics of droplet sizes generated by a microfluidic device, *AIChE J.* 62 (8) (2016) 2923–2928.
[35] D. Tsaoulidis, P. Angeli, Effect of channel size on liquid–liquid plug flow in small channels, *AIChE J.* 62 (1) (2016) 315–324.
[36] Z.Y. Liu, M.J. Chai, X. Chen, S.H. Hejazi, Y.Q. Li, Emulsification in a microfluidic flow-focusing device: effect of the dispersed phase viscosity, *Fuel* 283 (2021) 119229.
[37] A. Ładosz, P.R. von Rohr, Pressure drop of two-phase liquid–liquid slug flow in square microchannels, *Chem. Eng. Sci.* 191 (2018) 398–409.
[38] N.A. Mortensen, F. Okkels, H. Bruus, Reexamination of Hagen–Poiseuille flow: shape dependence of the hydraulic resistance in microchannels, *Phys. Rev. E Stat. Nonlin. Soft Matter Phys.* 71 (5 Pt 2) (2005) 057301.